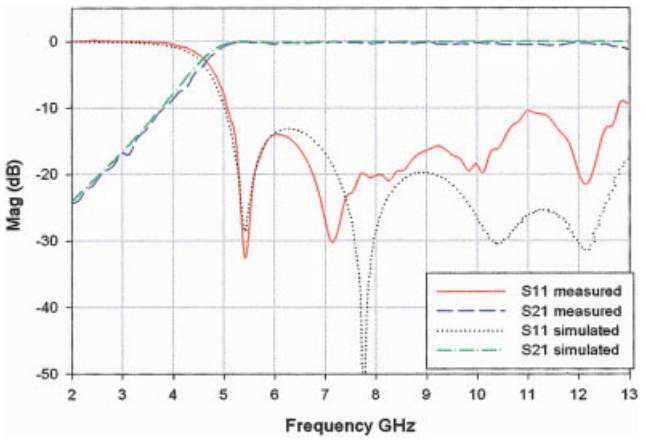

Figure 3 Response of the suspended coaxial transmission line. [Color figure can be viewed in the online issue, which is available at www.interscience.wiley.com.]

The different impedances needed for the suspended coaxial transmission line can be achieved by varying the size of the centre conductor [15]; here, the size of the outer conductor is fixed. The centre conductor of the resulting suspended coaxial transmission line is shown in Figure 2(a), with the cross-sections of the 50Ω line and the stubs shown in Figure 2(b). The input and output of the suspended transmission line, as shown in Figure 1, consist of 50Ω sections of transmission line.

For the coaxial assembly shown in Figure 1, layer 3 is 1-mm thick, and layers 2 and 4 are 2.25-mm thick. The complete device has an enclosed overall dimension of 45 × 20 × 5.5 mm. The five layers were clamped together for the experimental results given as follows.

3. RESULTS

The response of the suspended coaxial transmission line is shown in Figure 3; good agreement between theory and experiment is obtained. The transmission line was designed to work up to 13 GHz in a TEM mode; beyond this frequency, higher modes propagate through the structure, thus leading to a dispersive coaxial line. The suspended coaxial transmission line presented has low-loss transmission, and a usable frequency range from 5 to 13 GHz. The simulations were done according to [16]. The deviation of S_{11} from the simulations at the higher frequencies is probably due to a slight layer misalignment.

4. CONCLUSION

The layered air-filled coaxial cable discussed in this paper is a compact transmission line suitable for manufacture using micromachining technologies. The cable has been successfully demonstrated at the X-band, showing a low-loss wideband cable made out of five conducting layers. It is important to note that the structure allows the possibility of integrating other 3D structures made out of planar machined layers, such as filters, coupling structures, phase shifters, antennas, and delay lines.

REFERENCES

1. J.A. Bishop, M.M. Hashemi, K. Kiziloglu, L. Larson, N. Dagli, and U. Mishra, Monolithic coaxial transmission lines for mm-wave ICs, High speed semiconductor devices and circuits, Proc IEEE/Cornell Conf Adv Concepts, Ithaca, NY, 1991, pp. 252–260.
2. K.J. Herrick, T.A. Schwartz, and L.P.B. Katehi, Si-micromachined coplanar waveguides for use in high-frequency circuits, IEEE Trans Microwave Theory Tech 46 (1998), 762–768.
3. W.Y. Liu, D.P. Steenson and M.B. Steer, Membrane-supported CPW with mounted active devices, IEEE Microwave Wireless Compon Lett 11 (2001), 167–169.
4. J.-H. Park, C.-W. Baek, S. Jung, H.-T. Kim, Y. Kwon, and Y.-K. Kim, Novel micromachined coplanar waveguide transmission lines for application in millimetre-wave circuits Jpn J Appl Phys 39 (2000), 7120–7124.
5. P. Blondy, A.R. Brown, D. Cross and G.M. Rebeiz, Low-loss micromachined filters for millimetre-wave telecommunication systems, IEEE MTT-S Dig, Baltimore, MD (1998), 1181–1184.
6. J.E. Harriss, L.W. Pearson, X. Wang, C.H. Barron, and A.V. Pham, Membrane-supported Ka band resonator employing organic micromachined packaging, IEEE MTT-S Dig, Boston, MA (2000), 1225–1228.
7. H. Henri, S. Gonzague, V. Matthieu, C. Alain, and D. Gilles, Ultra low-loss transmission lines on low resistivity silicon substrate, IEEE MTT-S Dig, Boston, MA (2000), 1809–1812.
8. K. Takahashi, U. Sangawa, S. Fujita, M. Matsuo, T. Urabe, H. Ogura, and H. Yabuki, Packaging using microelectromechanical technologies and planar components, IEEE Trans Microwave Theory Tech 49 (2001), 2099–2104.
9. I. Llamas-Garro, K. Jiang, P. Jin, and M.J. Lancaster, SU-8 microfabrication for a Ka band filter, 4th Wkshp MEMS Millimiterwave Commun, Toulouse, France, 2003, pp. F55–F58.
10. S. Shimizu, K. Kuribayashi, M. Ohno, T. Taniguchi, and T. Ueda, Low-temperature reactive ion etching for bulk micromachining, IEEE Symp Emerging Technologies and Factory Automation, 1994, pp. 48–52.
11. C. Marxer, N.F. de Rooij, Micro-opto-mechanical 2 × 2 switch for single-mode fibers based on plasma-etched silicon mirror and electrostatic actuation. J Lightwave Tech 17 (1999), 2–6.
12. L. Gruner, Higher order modes in square coaxial lines, IEEE Trans Microwave Theory Tech 31 (1983), 770–772.
13. L. Gruner, Higher order modes in rectangular coaxial waveguides, IEEE Trans Microwave Theory Tech MTT-15 (1967), 483–485.
14. J.-S. Hong and M.J. Lancaster, Microstrip filters for RF/Microwave applications, Wiley, New York, 2001.
15. T.-S. Chen, Determination of the capacitance, inductance, and characteristic impedance of rectangular lines, IRE Trans Microwave Theory Tech 8 (1960), 510–519.
16. Ansoft HFSS. http://www.ansoft.com.

DUAL-FREQUENCY-SELECTIVE SURFACES FOR NEAR-INFRARED BANDPASS FILTERS

S. Govindaswamy,[1] J. East,[1] F. Terry,[1] E. Topsakal,[2] J. L. Volakis,[3] and G. I. Haddad[1]
[1] Solid State Electronics Laboratory
Electrical Engineering and Computer Science Department
University of Michigan
Ann Arbor, MI 48109
[2] Department of Electrical and Computer Engineering
Mississippi State University
Mississippi State, MS 39762
[3] Radiation Laboratory
Electrical Engineering and Computer Science Department
University of Michigan
Ann Arbor, MI 48109

Received 8 April 2004

ABSTRACT: *A bandpass filter resonating at ~1.4 μm and based on a dual-frequency-selective surface design is fabricated and characterized on a silicon substrate. The filter consists of square apertures arranged*

J.L. Volakis is also a Professor and the Director of ElectroScience Laboratory, Electrical Engineering Department, The Ohio State University, Columbus, OH 43212. E. Topsakal was formerly with the University of Michigan.

in a square lattice and separated by magnesium-fluoride dielectric layers. Simulations indicate minimal change in spectral reflectance versus overlay misalignment. The measured reflectance shows almost zero minima and a sharp roll-off. © 2004 Wiley Periodicals, Inc. Microwave Opt Technol Lett 43: 95–98, 2004; Published online in Wiley InterScience (www.interscience.wiley.com). DOI 10.1002/mop.20387

Key words: *arrays; bandpass filters; multilayer frequency-selective surfaces; electron-beam lithography; periodic structures*

1. INTRODUCTION

Multiple-layer frequency-selective surfaces (FSSs) stacked on top of each other can provide bandpass-filter characteristics that exhibit a flatter resonance and faster roll-off than single-layer structures [1]. The resonance between the multiple FSS can potentially reduce the reflection coefficient close to zero. Also, the FSS stack can be designed to provide a reduction in the change of bandwidth versus angle of incidence. An application of multiple FSS bandpass filters relates to the design of thermophotovoltaic (TPV) cells [2]. Thermophotovoltaic systems convert infrared radiation from a heat source into electricity using a low-bandgap semiconductor thermophotovoltaic cell. The radiation that can be absorbed has energy greater than that of the energy gap E_g of the semiconductor. FSSs can be used to improve the efficiency (output power versus incident photons) of a TPV system by placing it between the source and the TPV cell. The FSS reflects the radiations with a wavelength larger than the bandgap and transmits those with a wavelength just shorter than the bandgap wavelength with minimal absorption and reflection.

In this paper, a dual FSS layer filter resonating at $\sim$1.4 μm is presented. The effect of overlay misalignment between the FSS layers is studied, and the filter is characterized by measuring its reflectance spectrum for TE and TM excitations.

2. BANDPASS FILTER MODELING

The filter is modeled using the code FSDA_PRISM, as described in [3–5]. This code is based on a hybrid finite-element/boundary-integral (FE/BI) method for calculating the scattering by FSSs. It can also handle multiple commensurate and noncommensurate FSS layers. The filter consists of square apertures arranged in a periodic lattice. Ideally, the squares should have a linear width equal to about $\lambda/2$ and be separated by λ, where λ is the desired resonant wavelength. However, they must be scaled down if the filter is fabricated on top of a higher-index substrate. It is known that the metal thickness affects the response and our simulations take into account the effect of finite thickness and conductivity of the metal layer used to define the apertures [6]. The metal layer was defined as a dielectric layer within the finite-element region, with real and imaginary dielectric constants calculated from the refractive index from measurements available in the literature [7].

The schematic of the dual-FSS filter design is shown in Figure 1. Multiple MgF_2 layers are deposited on a silicon substrate and the FSSs are sandwiched between the dielectric layers. For our case, the FSS filter consists of square apertures arranged in a square lattice. It is defined on top of a dielectric layer, which has a lower refractive index than silicon. The dielectric material was assumed to be present inside and on top of the square apertures, with features scaled down by a factor of $\sim$1.4 as compared to a factor > 3 for a silicon substrate alone. The resultant dimensions are larger than those written directly on top of the silicon substrate and are thus easier to fabricate. In this design, square apertures of width equal to 440 nm with a spacing of 880 nm are required.

The simulations were done with a perfect electric conductor (PEC) to check the sensitivity of the spectral reflectance of the bandpass filter for overlaying misalignments. The reflectance for different misalignments along the x-axis was calculated for a TE excitation at 7° off-normal incidence and plotted in Figure 2(a). The measurements (given in section 4) were also made using a SOPRA GESP-5 ellipsometer at 7° off-normal incidence, operating in a photometry mode. The filters were assumed to consist of square apertures 440 nm in size and spaced 880-nm apart. Misalignment between the two layers is expected during lithography and a 100–160-nm variation is expected. A 60-nm misalignment represents a good case, whereas the 300 nm misalignment represents a worst-case scenario. There is minimal variation in the response for misalignments between 0 to 300 nm, and misalignment during fabrication should have minimal effect on the filter performance.

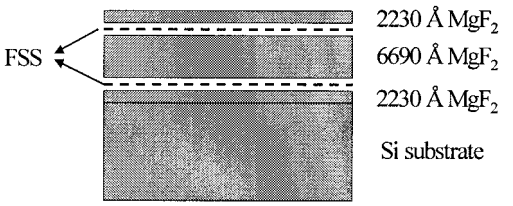

Figure 1 Schematic of the dual-FSS design

Simulations were done for the same misalignment along different axes. A 100-nm misalignment along the x-axis ($\theta = 0°$) and along $\theta = 45°$ was considered [Fig. 2(b)]. Again, there was minimal change in the spectral reflectance, except for the small

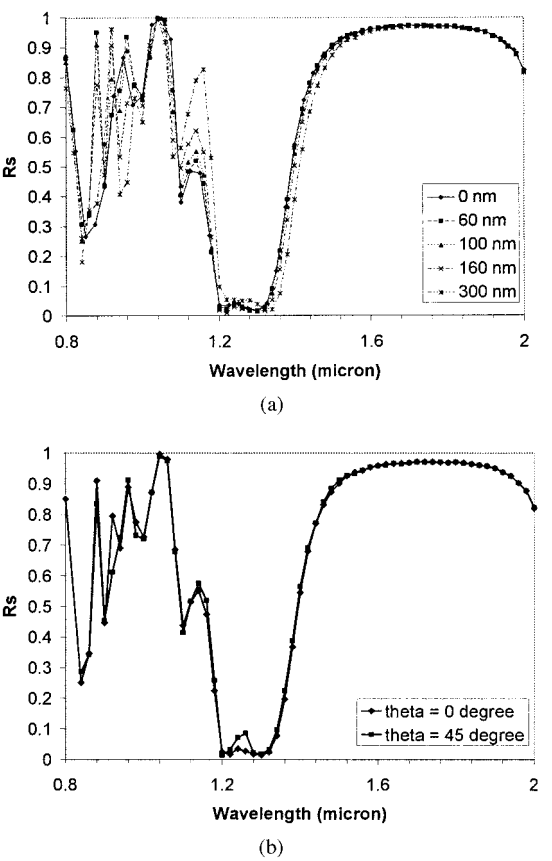

Figure 2 Simulated TE reflectance for an ideal dual-FSS bandpass filter for (a) different misalignments along the x-axis and (b) a 100-nm misalignment along different axes.

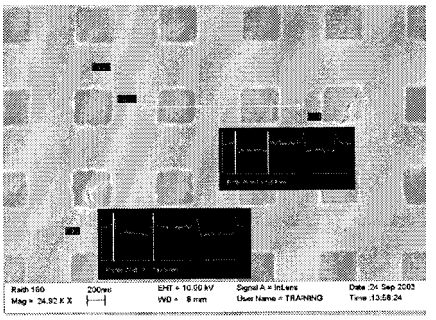

(a)

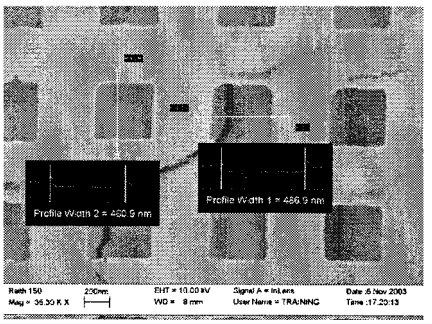

(b)

Figure 3 FSS apertures arranged in a square lattice: (a) bottom layer; (b) top layer

change in the local maximum near resonance. Clearly, in this design, a small misalignment did not affect the filter response appreciably. This lack of sensitivity reduces the alignment requirements during fabrication. For other cases, the simulations need to be performed in order to see the effect of misalignment.

3. FILTER FABRICATION

The filter was patterned using a bilayer resist consisting of 495K/950K PMMA. The pattern was written at 10-KeV acceleration voltage and an aperture of 30 μm, thus giving a beam current of ~200 pA. The working distance was set at 8 mm with a step size of 20 nm. The dosage was fixed at 100 μC/cm^2 and the writefield was 100 μm^2. The overall array size was ~800 × 800 μm^2 and some stitching errors were observed. A 40-nm-thick layer of aluminum was used to define the apertures. The final FSS dimensions were 435 × 435 nm and 460 × 485 nm for the bottom and top FSS arrays (see Fig. 3).

4. MEASUREMENTS

The reflectance of the filter was measured using a SOPRA GESP-5 Spectroscopic Ellipsometer in a photometer mode. The response for TE (R_s) and TM (R_p) excitations at 7° off-normal incidence were measured. For these measurements, we used a photomultiplier for the 0.5–0.9-μm wavelength range and then switched over to an extended InGaAs photodetector for the 0.9–2-μm wavelength range. The reference was an aluminum coating on a silicon wafer. The measurements were calibrated using a ~2-μm SiO_2 layer, also on a silicon wafer.

The spectral response shows slightly different behavior for TE and TM excitations (Fig. 4) and this is due to the slightly off-normal beam incidence (at normal incidence the response for both excitations would be identical). As designed, the spectrum shows a broad resonance between 1.3–1.5 μm with sharp roll-off. There is also a local maximum between the two minima; this is due to the

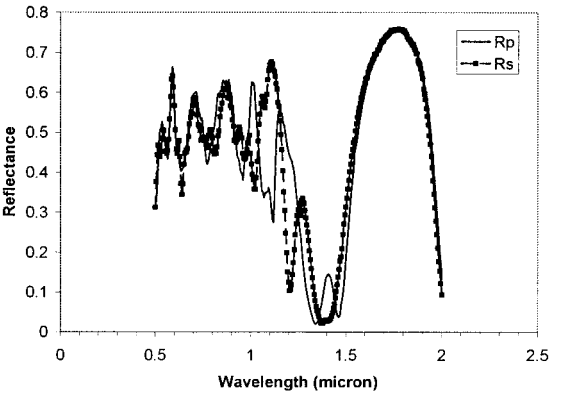

Figure 4 Measured reflectance of the dual-FSS bandpass filter for TE (R_s) and TM (R_p) excitations at 7° off-normal incidence

interaction of the two filters. This interaction is controlled by the thickness of the middle layer, and the design can be optimized to improve the flatness. We also observe that the reflection minima are close to zero, thus showing that the design is well matched at resonance. Overall, the bandwidth is ~25% and ~20% for TE and TM excitations, respectively. Nulls are observed at the shorter wavelengths and are due to the presence of grating modes. There is a null on the longer side of the resonance, but this can be removed by changing the thickness of the middle and top MgF_2 layer.

The initial simulation for the filter structure was done with the MgF_2 layer thicknesses specified in Figure 1. The actual feature sizes were used and a perfect overlay between the filters was assumed. The simulation was done for a TE excitation (see Fig. 5) and the angle of incidence was fixed at 7° off-normal. The results for a PEC are also shown for comparison. Overall, the measurements are in reasonable agreement with the simulations up to $\lambda \approx 1.7$ μm. For larger λ, the discrepancy between the simulation and measured data becomes larger. The PEC FSS resonates at a shorter wavelength and has better isolation.

We investigated the possible causes for the discrepancy at larger wavelengths. The variations in the dielectric constant ε or the thickness of the magnesium fluoride layers were considered. The dielectric constant of the magnesium fluoride layer was measured using ellipsometry. The refractive index was found to be ~1.39 and almost constant in the wavelength of interest. This is close to the value ($n = 1.4$) used in the simulation. Measurement of the dielectric layer

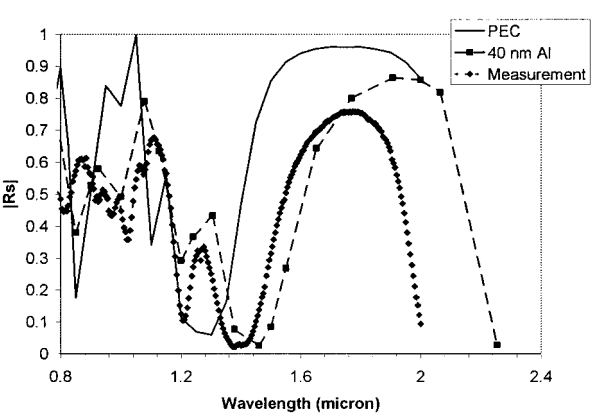

Figure 5 Simulated and measured responses of the dual-FSS filter for TE excitation at 7° off-normal incidence

thickness for the fabricated filter using ellipsometry indicated that it was ~8% thinner than the nominal case. Differences between the desired and actual thickness of the deposited layer could arise if the e-beam evaporator used for deposition is not calibrated well. The evaporator was calibrated using a dektak, and it is possible that the dektak was off by a few percent. Simulation with the aluminum layer and assuming that all layers were thinner by the same amount showed much better agreement with the measured result (see Fig. 6). This is true, especially for larger wavelengths where the disagreement was larger when the nominal case (Fig. 1) was assumed. It is possible that each layer varied from its nominal thickness rather randomly, and this could be another reason for the remaining differences between measured and calculated data. The PEC FSS simulation indicates a resonance at shorter wavelengths. Also, the PEC FSS has a better roll-off, but slightly higher reflection minima. Further, the local maximum between the two minima near the resonance is more pronounced for the TM excitations. This is damped in the measured data and the simulation with the metal layer. Nevertheless, the overall trend in the PEC simulation data follows that of the measured data.

This effect of the variation of layer thickness on the reflectance spectrum was confirmed by doing a sensitivity study. For ease of computation, the thicknesses of the layers were changed by the same fraction (see Fig. 7). The cases studied had −10%, −5%, and 5% variation for all the layers, as compared to the nominal case shown in Figure 1. The change in thickness affects the interaction between the two filters and in turn influences the local maxima between the two resonant minima. The agreement between simulation and measurements is better for the case of −10%. The simulations confirmed the fact that the variation in layer thickness was the reason for the discrepancy observed during the initial simulation.

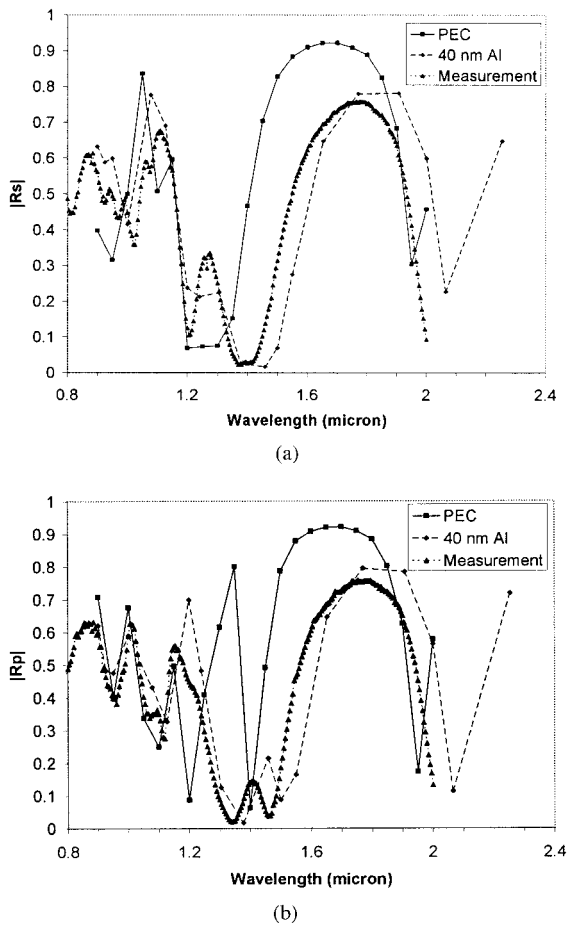

Figure 6 Simulated and measured responses of the dual-FSS filter with reduced thickness for (a) TE and (b) TM excitations at 7° off-normal indicence

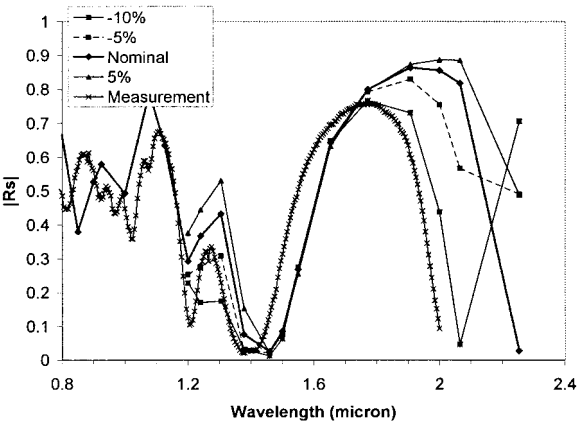

Figure 7 Simulated and measured responses of the dual-FSS filter with different dielectric layer thicknesses for TE excitation at 7° off-normal incidence

5. CONCLUSION

A near-infrared bandpass filter based on a dual-frequency-selective surface has been demonstrated. The simulations have shown that the design is not as sensitive to dimension variations, as a result of fabrication tolerances and misalignments. Measured reflectance data have also shown the desirable sharp roll-off and almost zero minima at the edges of the operational band, which agree well with the simulations once the effects due to finite metal thickness and conductivity are incorporated.

ACKNOWLEDGMENT

This work was supported by the Army Research Office (MURI program) under contract no. DAAG55-98-1-0288.

REFERENCES

1. B.A. Munk, Frequency-Selective Surfaces: Theory and Design, Wiley, New York, 2000.
2. R.E. Black, P.F. Baldasaro, and G.W. Charache, Thermophotovoltaics: Development status and parametric considerations for power applications, 18th Int Conf Thermoelectrics, 1999, pp. 639–644.
3. T.F. Eibert, J.L. Volakis, D.R. Wilton, and D.R. Jackson, Hybrid FE/BI modeling of 3D doubly periodic structures utilizing triangular prismatic elements and an MPIE formulation accelerated by the Ewald transformation, IEEE Trans Antennas Propagat 47 (1999), 843–850.
4. T.F. Eibert and J.L. Volakis, Fast spectral domain algorithm for hybrid finite element/boundary integral modeling of doubly periodic structures, IEE Proc Microwave Antennas Propagat 147 (2000), 329–334.
5. T.F. Eibert, Y.E. Erdemli, and J.L. Volakis, Hybrid finite element-fast spectral domain multilayer boundary integral modeling of doubly periodic structures, IEEE Trans Antennas Propagat 51 (2003), 2517–2520.
6. E. Topsakal and J. Volakis, On the properties of materials for designing filters at optical frequencies, IEEE Antennas Propagat Soc Int Symp Dig 4 (2003), 635–638.
7. E.D. Palik, Handbook of optical constants of solids, Academic Press, Orlando, FL, 1985.